Characteristic properties of the microstructure and microtexture of medium-carbon steel subjected to sulfide stress cracking

Andrey V. Malinin[*1,3], PhD (Engineering),
Deputy Director
Vil D. Sitdikov[1,4], Doctor of Sciences (Physics and Mathematics),
Head of the laboratory
Valeria E. Tkacheva[1,5], PhD (Engineering), Associate Professor, Chief Specialist
Artem K. Makatrov[1,6], PhD (Engineering),
Head of the Department
Ilya V. Valekzhanin[1,7], Head of the Department
Andrey N. Markin[2], PhD (Engineering),
assistant professor of Chair "Oil and Gas Engineering"

[1]*LLC "RN-BashNIPIneft", Ufa (Russia)*
[2]*Branch of Industrial University of Tyumen in Nizhnevartovsk, Nizhnevartovsk (Russia)*

*E-mail: MalininAV@bnipi.rosneft.ru

[3]ORCID: https://orcid.org/0000-0003-1185-5648
[4]ORCID: https://orcid.org/0000-0002-9948-1099
[5]ORCID: https://orcid.org/0000-0001-6927-9781
[6]ORCID: https://orcid.org/0000-0002-2822-9072
[7]ORCID: https://orcid.org/0000-0001-9472-2968

Abstract: Increasing the resistance of steel products to sulfide stress cracking (SSC) is one of the topical issues of the oil and gas industry. Among various factors determining the SSC resistance of a material is the structure-phase state of the material itself and the crystallographic texture associated with it. The current paper analyzes these features using the scanning electron microscopy (SEM), transmission electron microscopy (TEM), and microroentgen electron backscattered diffraction (EBSD) techniques. As the research material, a production string (PS) coupling made of medium-carbon steel was selected, which collapsed by the mechanism of hydrogen embrittlement and subsequent SSC. For the first time, by the SEM method, using the location and mutual orientation of cementite (Fe_3C) particles, at high magnifications, the authors demonstrated the possibilities of identifying the components of upper bainite, lower bainite, and tempered martensite in steels. The presence of the detected structural components of steel was confirmed by transmission electron microscopy (TEM). Using the EBSD method, the detailed studies of microtexture were conducted to identify the type and nature of the microcrack propagation. It is established that the processes of hydrogen embrittlement and subsequent SSC lead to the formation of $\{101\}$ $<0\bar{1}0>$, $\{100\}$ $<001>$, $\{122\}$ $<2\bar{1}0>$, $\{013\}$ $<211>$, $\{111\}$ $<\bar{1}00>$, $\{133\}$ $<\bar{1}\bar{2}1>$, $\{3\bar{2}\bar{6}\}$ $<201>$ grain orientations. It is shown that the strengthening of orientations of $\{001\}$ $<110>$, $\{100\}$ $<001>$, $\{112\}$ $<111>$, and $\{133\}$ $<\bar{1}\bar{2}1>$ types worsens the SSC resistance of the material. Using the EBSD analysis method, the influence of special grain boundaries on the nature of microcrack propagation is estimated. It is found that the Σ 3 coincident site lattice grain boundaries between the $\{122\}$ $<2\bar{1}0>$ and $\{111\}$ $<\bar{1}00>$, $\{012\}$ $<\bar{1}\bar{1}0>$, $\{100\}$ $<001>$ plates of the upper bainite inhibit the microcrack development, and the Σ 13b, Σ 29a, and Σ 39a boundaries, on the contrary, contribute to the accelerated propagation of microcracks. For comparative analysis, similar studies were carried out in an unbroken (original) coupling before operation.

Keywords: medium-carbon steel; bainite microstructure; sulfide stress cracking; crystallographic texture.

INTRODUCTION

The complex of oil and gas pipes of the Russian Federation is one of the most developed systems, and belongs to the key type of raw oil and gas transportation throughout the RF territory. In this regard, the highest requirements are imposed on oil and gas pipelines, which aim to ensure their reliability, durability, and safety [1–3]. The latter is associated with irreversible environmental, and economic expenditures in the case of an unintended breakdown of pipelines and their units in a certain sector of oil transportation. Among various types of complications in oil production, the mechanical corrosion failure – sulfide stress cracking is the most serious [4–6]. Sulfide stress cracking (SSC) of oilfield equipment is determined by the action of various factors, among which are the partial pressure of hydrogen sulfide and the temperature in the string, the degree of salinity of the water component of oil, and the stress-strain state of the metal. These factors are best described in the GOST 53678 standard and in the works [6–8]. Besides the abovementioned factors, the SSC-resistance of steels is determined by the degree of alloying of iron with impurity atoms, the structure-phase state, the level and anisotropy of strength properties, which determine

the final mechanical properties of materials. A developed crystallographic texture, which can be controlled by optimizing the modes of thermomechanical effect, is a particularly important parameter in the operation of goods [5; 9].

It is known that the boundaries of grains, laths, and plates formed during quenching and subsequent tempering, are the preferred areas for precipitation of cementite particles [10]. As a result of external applied loads, due to the difference in microhardness, microcracks appear between the cementite particles and the main matrix. Subsequently, they propagate along the prior austenite grain boundaries (PAGB) or along the lath martensite boundaries [10]. According to [11], martensitic steel characterized by a relatively low ductility is more prone to SSC compared to tempered martensite. At the same time, the presence of some alloying elements (for example, Nb, V, Mo, and Ti) during aging generates the precipitate at the grain boundaries, which reduce the SSC susceptibility of steel [11]. The shape and size of the constituent elements of the steel microstructure also determine the material propensity to SSC. In particular, the authors [12] identified that the ferrite-pearlite structure is more prone to SSC than the acicular ferrite or ultrafine-grained bainitic structure. In this regard, it was concluded that a homogeneous and uniform structure has a greater SSC resistance [12].

Some works deal with the study of the nature of the microcrack propagation in steels, as well as identifying the relationship between this nature and the crystallographic texture, the type of grain boundaries and their orientation relative to each other [13–15]. In particular, in the work [13], the authors showed that the formation of low-angle and coincident site lattice (CSL) grain boundaries increases the cracking resistance of the API X65 steel. Moreover, it was found that the presence of CSL grain boundaries smaller than Σ 13b provides cracking resistance [13], while a number of other high-angle boundaries (not CSL), worsen the SSC resistance [14; 15]. As a result, forming the low-angle and CSL grain boundaries of a certain type, it is possible to stop a microcrack after its formation and obtain crack-resistant steel.

Thus, the above factors, which are responsible for the microcrack initiation and development, are controlled, and on the whole, determine the tendency of the material to SSC. The control of these factors, by changing the processing parameters, as well as the formation of certain microstructures and crystallographic textures with the required strength characteristics for specific types of operation of oilfield equipment, is a crucial task.

This work is aimed to identify the structure-phase features and regularities of the texture formation processes, in a standard production string coupling made of bainitic steel structure, as well as to establish the factors determining its resistance to hydrogen sulfide stress cracking.

METHODS

A production string (PS) coupling with an outer diameter of 139.7 mm and a wall thickness of 9.17 mm, manufactured according to the GOST 31446 standard (strength group P110), was selected as the research material. The chemical composition of the investigated coupling is shown in Table 1.

The studies were carried out in two PS couplings. The first one was destroyed by the SSC mechanism during the hydraulic fracture of a shelf on an exploration well. The second coupling was new, without operation. A bainite structure was formed in the couplings at the factory conveyor conditions, by carrying out the traditional heat treatment (quenching and subsequent tempering). The mechanical tensile tests were carried out using an INSPEKT 200 universal testing machine according to the GOST 10006 requirements. Microhardness was measured by the Rockwell method using a 251 VRSD universal hardness tester. The SP coupling microstructure was studied using a Thermo Scientific Q250 scanning electron microscope equipped with the EDAX-TSL system for backscattered electron diffraction (EBSD) analysis. The imaging of samples was carried out at an accelerating voltage of 20 kV at a chamber pressure of 10^{-4} Pa. The electron beam diameter was 3 μm. During the study, the sample was placed at a focal distance of 10.0 mm. Nital solution was used as a metallographic reagent. The microstructure was also analyzed using a transmission electron microscope (TEM), to get the information about the size of structural elements and the nature of the arrangement of cementite precipitates. The observations were carried out on a JEM-2100 microscope at an accelerating voltage of 200 kV. The samples for TEM were prepared by two-jet electropolishing using an electrolyte based on n-butyl alcohol.

Table 1. Chemical composition of the coupling material
Таблица 1. Химический состав материала муфты

Content, wt.%									
Fe	**C**	**Si**	**Mn**	**P**	**S**	**Cr**	**Ni**	**Mo**	**Al**
97.1	0.452	0.306	1.400	0.014	0.005	0.278	0.199	0.006	0.012
Content, wt.%									
Co	**Cu**	**V**	**Ti**	**Sn**	**B**	**Zr**	**As**	**Bi**	
<0.001	0.026	0.058	0.002	0.011	0.002	0.002	0.075	0.010	

RESULTS

The average value of the coupling metal microhardness in the primary crack nucleus is 35.5 HRC, and far from the crack, its value decreases to 34.0 HRC. At the same time, the average hardness of the pipe billet metal without operation was 32.6 HRC. The mechanical tests showed that in the coupling before operation, the tensile strength was 983 MPa, the yield strength was 913 MPa, and the relative elongation was 15.5 %; while after operation, the tensile strength was 1096 MPa, the yield strength was 1000 MPa, and the relative elongation was 13.7 %.

Fig. 1 a shows a typical SEM image of the PS coupling microstructure (before operation) after etching. The experimental microstructure is mainly characterized by a bainitic structure consisting of parallel plates. In the photograph, the bainite plates are shown as disoriented blocks inside the PAGB (Fig. 1 a). The bainitic blocks in Fig. 1 a in some places are circled by green contour lines, and PAGB – by yellow lines. Along with the bainite component, the microstructure contains the irregularly shaped islands of the martensitic-austenitic (M/A) phase (Fig. 1 a). Unlike the bainite component, the M/A areas are resistant to etching; they look like non-etched and relatively light areas (outlined with a white line) (Fig. 1 a). A microstructure detailed analysis at rather high magnifications showed that the bainite component is formed from the upper bainite (UB) and lower bainite (LB) plates. This fact is supported by the results of SEM and TEM studies, according to which the needle-like cementite (Fe_3C) particles in the UB plates are located only at the plate boundaries and are oriented along the boundaries (Fig. 1 b) [10]. The detected cementite particles at the boundaries of the UB plates in some places grow up to a length of 170 nm, while their diameter equal to ~34 nm remains practically unchanged. At the same time, in the LB, cementite particles are formed only in the body of the plates (Fig. 1 c, 1 d). In this case, the cementite particles in the LB have a needle-like shape (up to 210 nm long, 22 nm in diameter) and are parallel to each other (Fig. 1 c, 1 d). Fig. 1 d shows the section of the "coalesced" LB, where the merge of parallel plates is observed. In the PS coupling microstructure, rather large plates of tempered martensite (TM) are observed in some places (Fig. 1 e, 1 f). Similar structural components (LB, UB, and TM) in steels were previously observed in the works [17–19]. The TM plates (laths) have a length of up to several tens of microns and a width of 1–4 microns. The difference between the TM and the UB and LB is that, in the TM plates, cementite particles of the needle-like morphology are oriented between themselves both parallel and at an angle of 60° with respect to each other (Fig. 1 e, 1 f) [19].

Fig. 2 a shows a typical SEM image of the PS coupling microstructure after operation. The precision SEM analysis showed (Fig. 2 a, 2 b) that the microstructure of the PS coupling after operation contains similar structural components (UB, LB, TM, and M/A), which were found in the original coupling (Fig. 2 a–f). At the same time, during the transition to the area where the destruction occurred according to the SSC mechanism, significant changes in the microstructure are identified (Fig. 2 c–f).

In particular, in the area very close to a fracture, the microstructure is characterized by the absence of visible needle-like cementite particles in the plates (laths) (Fig. 2 c).

The absence of cementite particles both inside the plates and between them indicates the formation of a purely martensitic structure with a body-centered tetragonal (BCT) lattice [20]. The external applied load in the fracture zone leads both to the rotation of the plate-like structure in the direction of tensile forces and the formation of deformation bands (Fig. 2 d) and to the appearance of cracks on the non-metallic inclusions (Fig. 2 d, upper right corner, Fig. 2 e, upper left corner). Fig. 2 e, 2 f show a general view of the path of the secondary crack propagation as a result of SSC. It is obvious that at the initial stages, the crack propagates according to the transcrystalline type (up to 60 μm), and then it has an intercrystalline type (Fig. 2 e, 2 f). In this case, it is seen that, when stopped, a crack can be initiated at the boundary of the plates (Fig. 2 f). The analysis of SEM images showed that in all the studied areas, the PS coupling contamination with non-metallic inclusions did not exceed 5 points (SH method).

To analyze the nature of microcrack propagation, the authors studied the local crystallographic microtexture, i. e., the predominant grain orientations, as shown in Fig. 3 a. The analysis of the distribution map of grain orientations was carried out in the plane of the sample cross section. For ease of analysis, individual orientations of each block and plates are shown in different colors (Fig. 3 a, 3 b).

According to the EBSD analysis, the average size of the PAGB blocks in the PS coupling before operation was ~80 μm, and after failure in the fracture region, it was ~66 μm. The EBSD analysis showed that, in the coupling failure area, a crystallographic texture is basically formed, in which grain orientations related to the {101} <010>, {100} <001>, and {111} <$\bar{1}$00> texture components dominate (Fig. 3 a). At the same time, in the coupling without operation, the {110} <001>, {001} <110>, and {111} <011> grain orientations are prevailing. The main texture components identified in the PS coupling before and after operation (with a crack) are recorded in Table 2.

Besides, Table 2 shows schematically the orientations of individual plates with respect to the ND–TD plane and their volume fractions belonging to one or another texture component. To identify the influence of the texture formation processes on the nature of crack propagation, local EBSD studies were carried out (Fig. 3 b). In this case, the authors paid special attention to the identification of high-angle disorientations related to CSL grain boundaries formed both in the original coupling and in the coupling after operation (Fig. 4 a, 4 b). The distributions of CSL grain boundaries corresponding to the original and destroyed coupling (crack area) are shown in Fig. 4 a, 4 b, and their volume fractions are summarized in Table 3.

To determine the influence of mutual orientations of plates (laths) on the crack propagation character, the authors carried out an analysis of microtexture research. Fig. 5 shows the direct pole figures (PF) (110) of the PS coupling obtained from different areas of analysis: without operation, away from the fracture, and in the crack surrounding area.

The pole figure (110) obtained for the PS coupling be-fore operation, according to microtexture analysis, is characterized by a set of the following main orientations: {101} <0$\bar{1}$0>, {100} <001>, {122} <2$\bar{1}$0>, {013} <211>, {111} <$\bar{1}$00>, {133} <$\bar{1}\bar{2}$1>, {3$\bar{2}\bar{6}$} <201>, {102} <2$\bar{1}$1>, {230} <323>, {122} <2$\bar{2}$1>, {110} <1$\bar{1}$1>, and {111} <$\bar{1}$00>
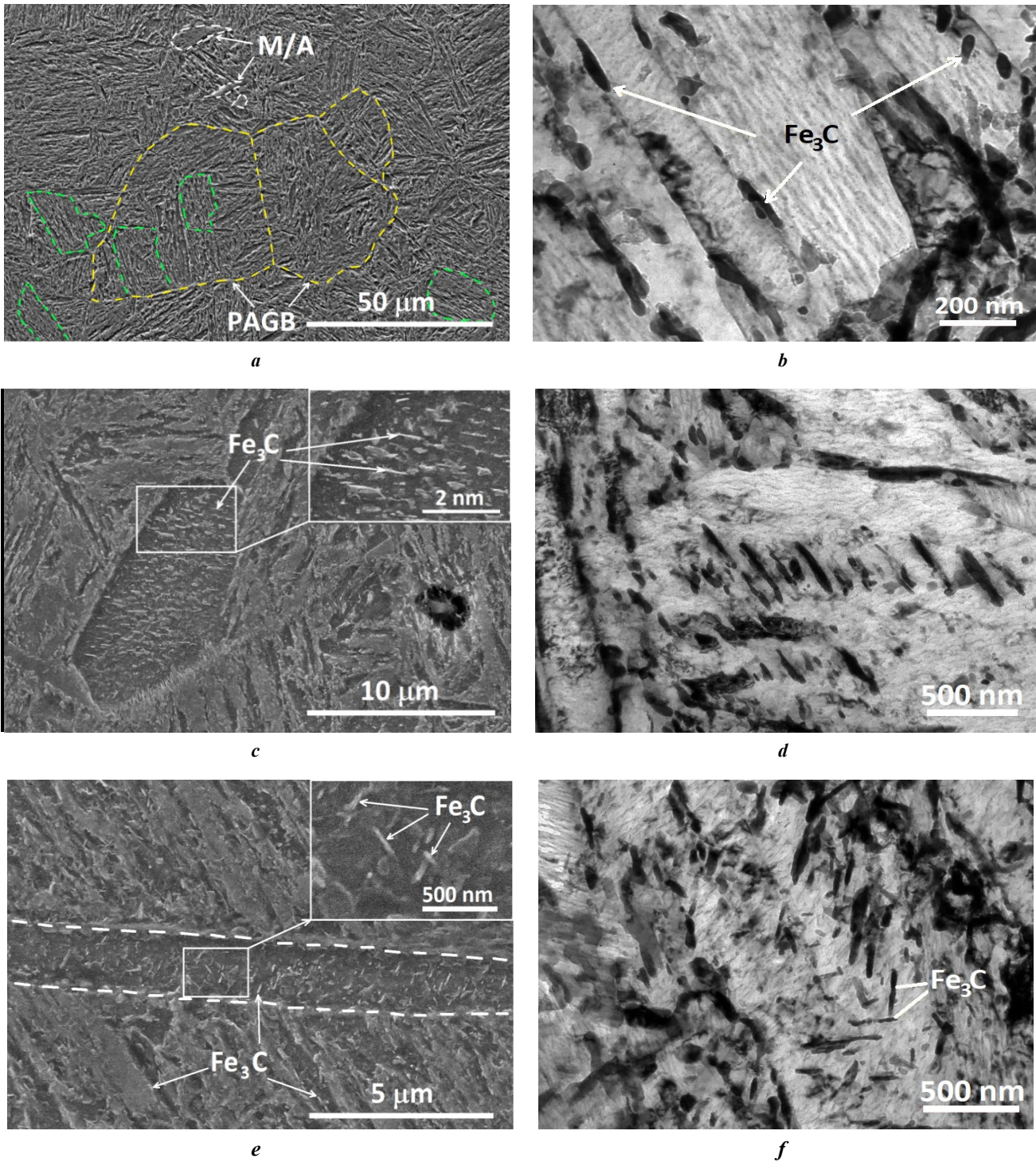
Fig. 1. Images of the PS coupling microstructure (before operation):
a – microstructure general view; b – upper bainite plates;
c, d – lower bainite plates; e, f – martensite tempering plates.
M/A – martensite-austenite areas; PAGB – prior austenite grain boundaries.
a, c, e – SEM images; b, d, f – TEM images
Рис. 1. Изображения микроструктуры муфты ЭК (до эксплуатации):
a – общий вид микроструктуры; b – пластины верхнего бейнита;
c, d – пластины нижнего бейнита; e, f – мартенситные пластины отпуска.
M/A – мартенситно-аустенитные участки; PAGB – первоначальные границы зерен аустенита.
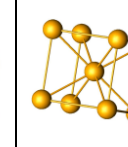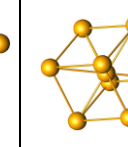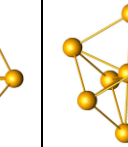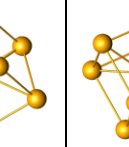*a, c, e – РЭМ-изображения; b, d, f – ПЭМ-изображения*
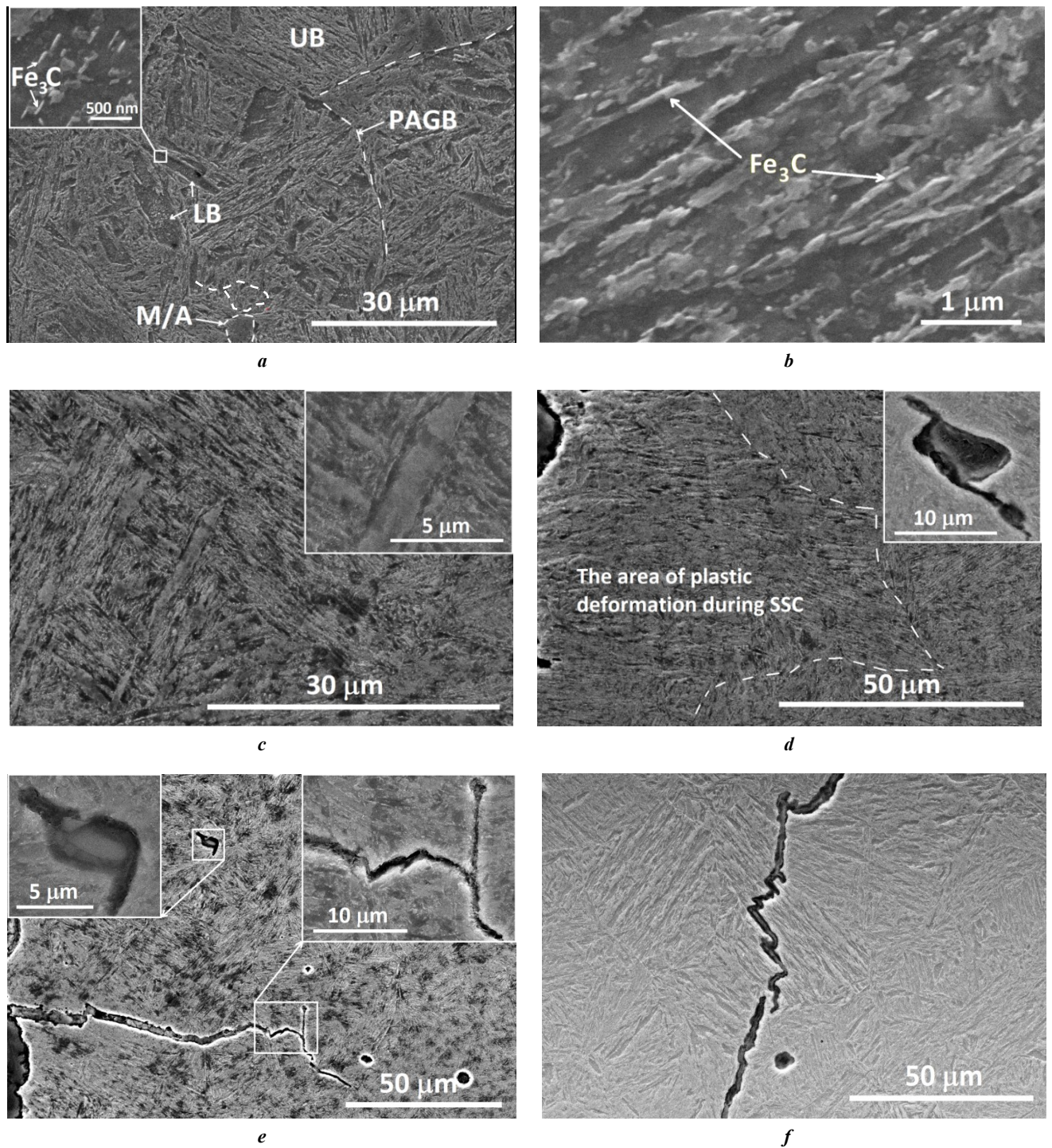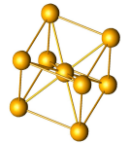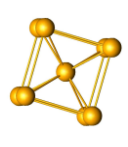
Fig. 2. *Microstructure SEM images:*
a *– general view of the microstructure away from the fracture area;* ***b*** *– upper bainite plates;*
c *– general view of the microstructure in the fracture area;* ***d*** *– deformation bands;*
e *– the appearance of cracks in the fracture area;* ***f*** *– crack development on bainitic blocks.*
UB – upper bainite; LB – lower bainite
Рис. 2. *РЭМ-изображения микроструктуры после эксплуатации:*
a *– общий вид микроструктуры вдали от излома;* ***b*** *– пластины верхнего бейнита;*
c *– общий вид микроструктуры в области излома;* ***d*** *– полосы деформации;*
e *– вид трещин в области излома;* ***f*** *– развитие трещины на бейнитных блоках.*
UB – верхний бейнит; LB – нижний бейнит

Table 2. *The determined orientations of bainite/martensite plates and their volume fraction*
Таблица 2. *Обнаруженные ориентации бейнитных/мартенситных пластин и их объемная доля*

Plane of Analysis ↑ND →TD	The main orientations and their volume fraction, %						
	🟩	🟥	🟦	🟧	🔵	🟩	🟪
Euler angles, φ_1, Φ, φ_2	181.8, 35.1, 76.7	88.2, 5.9, 73.7	230.2, 46.5, 66.4	259.6, 13.5, 0	333.9, 49.1, 49.8	17.6, 44.5, 17.9	331.3, 33.4, 55.5
Orientation	{101} <0$\bar{1}$0>	{100} <001>	{122} <2$\bar{1}$0>	{013} <211>	{111} <$\bar{1}$00>	{133} <$\bar{1}$21>	{3$\bar{2}$$\bar{6}$} <201>
Before operation	4.6	3.3	4.1	6.5	6.5	7.8	8.9
After operation	8.2	6.9	7.2	8.8	6.0	12.3	5.7
Crack area	9.9	13.7	9.1	12.1	8.6	10.2	4.6

Note. ND – normal direction oriented along the coupling (pipe) radius;
TD – transverse direction coinciding with the coupling (pipe) axis.

Примечание. ND – нормальное направление, ориентированное вдоль радиуса муфты (трубы);
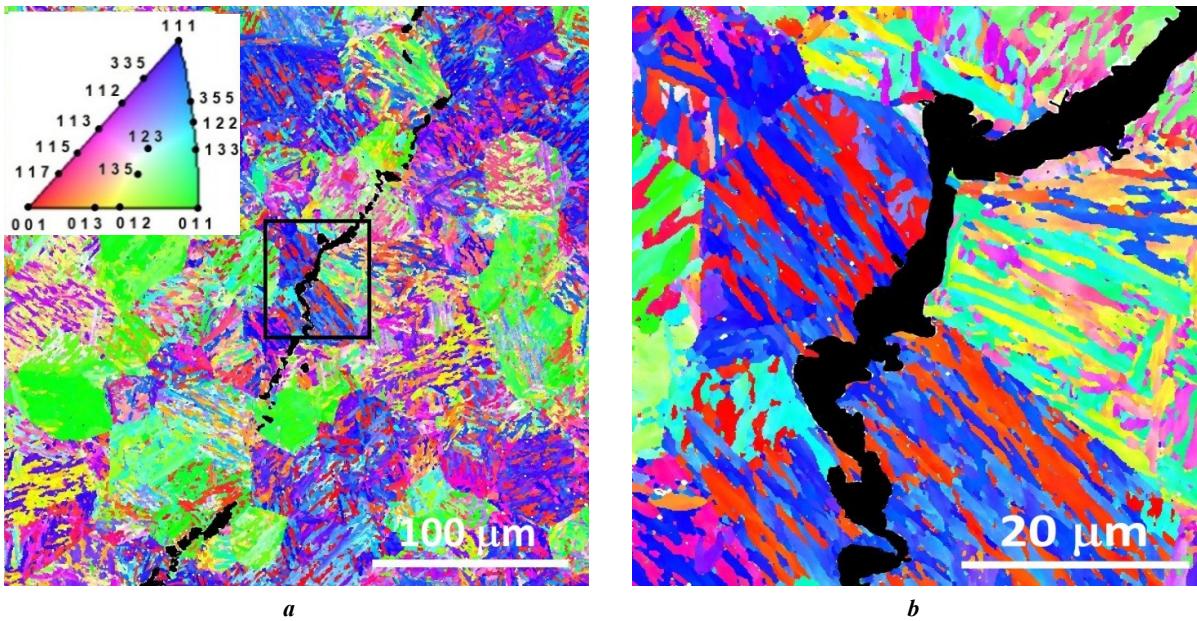*TD – поперечное направление, совпадающее с осью муфты (трубы).*

Fig. 3. *EBSD images of the microstructure: **a** – general view; **b** – precision area*
Рис. 3. *ДОРЭ-изображения микроструктуры: **a** – общий вид; **b** – прецизионный участок*
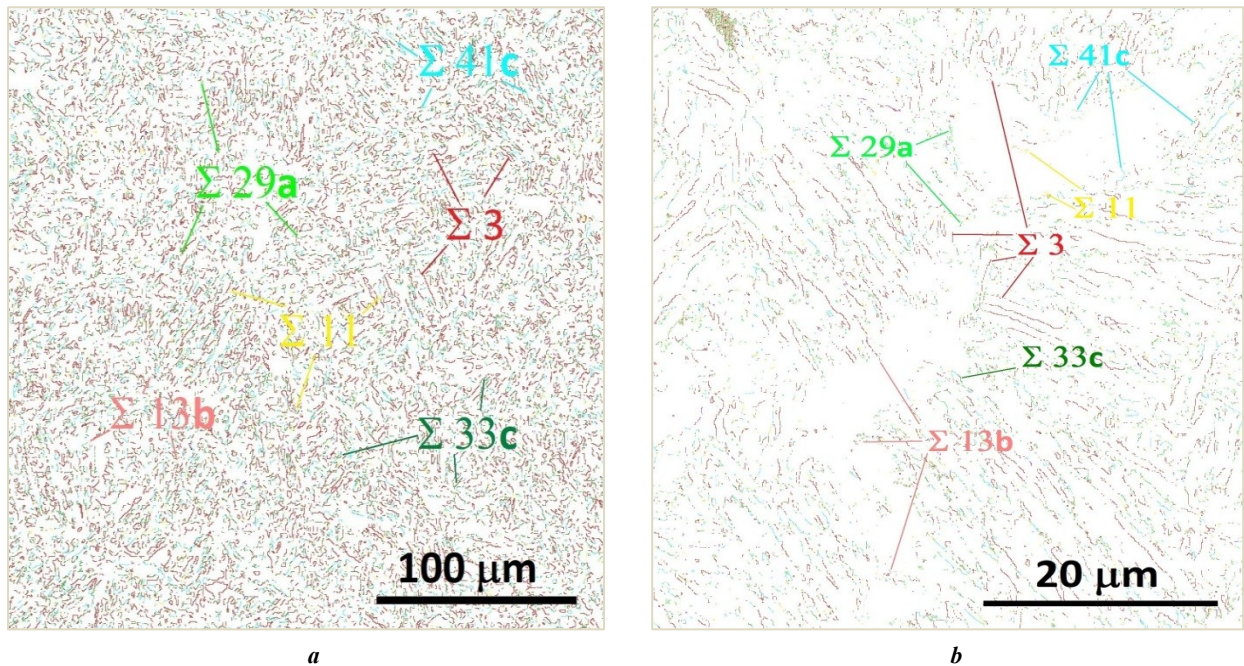
Fig. 4. *EBSD images of the microstructure:*
a *– map of distribution of special grain boundaries in the coupling (pipe) without operation;*
b *– map of distribution of special grain boundaries in the crack area*
Рис. 4. *ДОРЭ-изображения микроструктуры:*
a *– карта распределения специальных границ зерен в муфте без эксплуатации;*
b *– карта распределения специальных границ зерен около трещины*

Table 3. *The revealed CSL grain boundaries of bainite plates and their volume fraction*
Таблица 3. *Выявленные специальные границы Σ бейнитных пластин и их объемная доля*

The area of analysis	Volume fraction of CSL grain boundaries, %							
	Σ 3	Σ 11	Σ 13b	Σ 25b	Σ 29a	Σ 33c	Σ 39a	Σ 41c
Before operation	12.4	1.1	0.4	1.1	0.3	4.3	0.8	4.2
After operation	11.9	1.4	0.2	1.3	0.1	5.0	0.3	3.8
Crack area	9.6	3.6	4.4	0.4	2.3	2.2	2.6	3.9

(Fig. 5, Table 2). Since the microtexture analysis covers the study of the crack development nature, Fig. 5 d and Table 2 show only the positions of the main grain orientations. The analysis showed that in the PS coupling after operation (away from the crack), the general appearance of the (110) PF remains. However, the ratio of the preferred grain orientations changes. This is evidenced by the redistribution of texture maxima on the (110) PF, where the $\{102\}$ $<2\bar{1}1>$, $\{230\}$ $<323>$, $\{122\}$ $<2\bar{2}1>$, $\{110\}$ $<1\bar{1}1>$ and $\{111\}$ $<\bar{1}00>$, and $\{111\}$ $<\bar{1}00>$ orientations are suppressed, while the $\{101\}$ $<0\bar{1}0>$, $\{100\}$ $<001>$, $\{013\}$ $<211>$, $\{122\}$ $<2\bar{1}0>$, and $\{133\}$ $<\bar{1}\bar{2}1>$ texture components are enhanced (Fig. 5 b, Table 2). This fact is explained by the fact that during operation, the structure elements rotate as a result of the action of the applied external loads. Moreover, additional orientations (textural maxima) appear on the (110) PF and the pole density of some orientations sharply increases (Fig. 5 b). In particular, as a result of SSC, the weight fractions of the $\{001\}$ $<110>$, $\{100\}$ $<001>$, $\{112\}$ $<111>$, and $\{133\}$ $<\bar{1}\bar{2}1>$ texture components increase (Fig. 5 b).

The precision microtexture analysis showed that the nature of the location of texture maxima on the (110) PF in the crack area changes significantly (Fig. 5 c). In this case, an increase in the pole density of individual orientations is observed (Fig. 5 c). In particular, in the zone
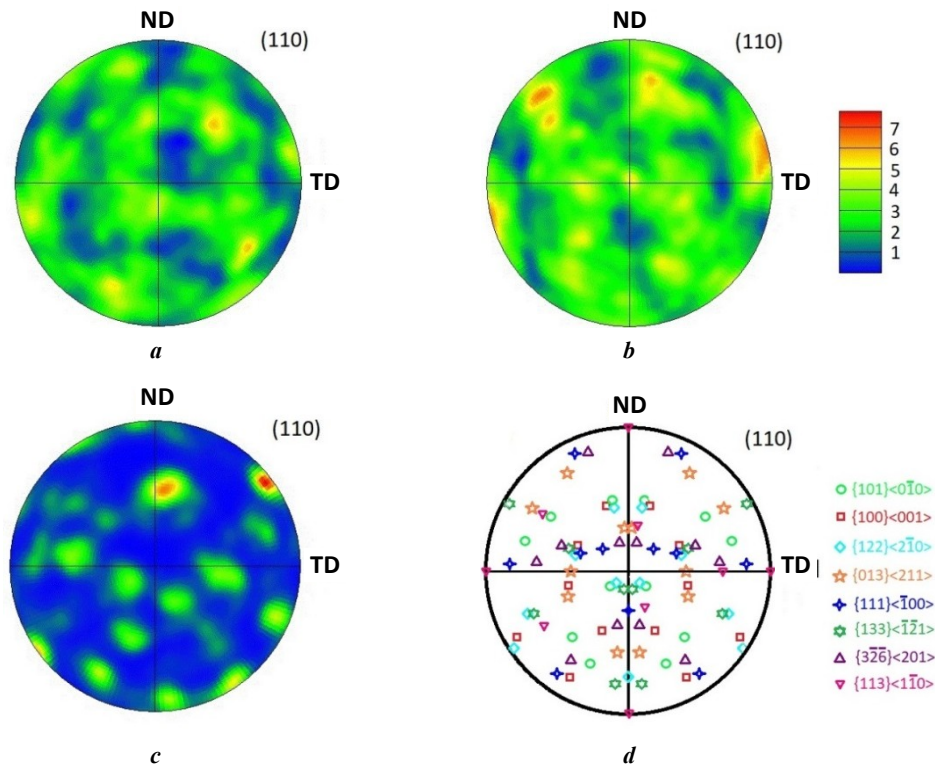
Fig. 5. *Direct pole figures (110):*
a *– PS coupling before operation;* ***b*** *– after operation away from the crack;*
c *– in the crack area;* ***d*** *– the positions of the determined orientations on a pole figure*
Рис. 5. *Прямые полюсные фигуры (110):*
a *– муфта ЭК до эксплуатации;* ***b*** *– после эксплуатации вдали от трещины;*
c *– в области трещины;* ***d*** *– позиции обнаруженных ориентаций на полюсной фигуре*

of crack development, there is a sharp increase in the $\{101\}$ $<0\bar{1}0>$, $\{100\}$ $<001>$, $\{122\}$ $<2\bar{1}0>$, and $\{133\}$ $<\bar{1}\bar{2}1>$ grain orientations, uncharacteristic for the initial PS coupling. In general, the changes in the (110) PF, on the one hand, are associated with the formation of an unfavorable crystallographic texture, and, on the other hand, with the active processes of grinding bainite blocks and subsequent reorientation of the plates as a result of shear deformations.

DISCUSSION

The analysis of the microstructure of the medium-carbon steel PS coupling showed that various structure components are formed in it: upper bainite, lower bainite, and tempered martensite (Fig. 1). These structural components differ both by the arrangement of cementite particles and their mutual orientation, and by the dimensions of the plates (laths). In particular, the average width of the UB plates is 0.7 μm, and the length is ~25 μm. Cementite particles in the UB plates are located along their boundaries [16–18]. Compared to the UB, the width of the plates in the LB is a bit narrower (0.5 μm), and their length does not exceed 20 μm. Needle-like cementite particles in the LB precipitate in the body of the plates and are strictly parallel to each other [16–18]. In the tempered martensite plates, the cementite particles precipitate in the form of needles located in the body of the plates (laths) and are oriented to each other both in parallel and at an angle of 60° with re-

spect to each other [19]. This fact indicates that cementite particles can grow along the <011> and <110> directions in the BCT lattice. The length of the cementite particle inside the TM plates reaches 300 μm, and the diameter is ~39 μm.

Thus, the UB, LB, and TM distinguishing features are the dimensions of the plates, the precipitation area of cementite particles on the plates, and their mutual orientation. Cementite particles in the UB precipitate only at the boundaries of the plates (laths), in the LB, they precipitate only inside the plates and are parallel to each other, and in the TM plates they are oriented at an angle to each other.

The analysis of the microstructure identified the presence of a structural gradient (UB, LB, TM, M/A, and martensite) in the PS coupling material. In particular, in the area close to the fracture, many martensite plates were found, which, apparently, locally increase the microhardness to 35.5 HRC. Martensite plates in the fracture area are characterized by the absence of cementite particles, the lath width in the range of 0.6–3.5 μm, and the length of a few tens of μm. At the same time, areas with a high content of martensite/austenite component of irregular shape were found as well in this area. Numerous secondary microcracks are observed in the fracture area, since the martensitic structure is less SSC-resistant and requires additional tempering [21].

The analysis of the general appearance and path of the secondary crack propagation as a result of SSC indicates that the nature of crack development can be divided into two

stages. At the first stage, it propagates along a rather straight trajectory. It is obvious that the crack thickness, which is approximately equal to 7.5 μm at the crack tip, remains virtually unchanged up to large depths (more than 60 μm) (Fig. 2 e). This fact indicates that up to the depths of 60 μm, corrosion processes are actively realized with the formation of iron oxides/sulfides. Further, the crack has a more tortuous propagation pattern containing a greater number of deflections (Fig. 2 e, 2 f). At the same time, at the initial stage, the type of crack propagation is transcrystalline (Fig. 2 e). Changes in the microstructure caused by the action of tensile stresses, and the formation of deformation bands shown in Fig. 2 d also led to this type of crack propagation. In this case, the deformation bands were formed as a result of the bainitic structure rotation in the direction of the action of tensile forces perpendicular to the fracture propagation line (Fig. 2 d, 2 e). The front of deformation bands reaches great depths and sometimes amounts to several hundred microns. As a result, in such areas, cracks easily propagate parallel to the dislocation slip lines, since there are no obstacles in their path. However, if a crack encounters in its path the transversely located bainite blocks, then it starts to slow down on them, as shown in Fig. 2 f. At the same time, the action of high applied tensile stresses sometimes leads to the initiation of secondary cracks in the areas close to the zone where the primary crack stops. Such areas are the MnS inclusions, spherical voids, PAGBs, and a favorable crystallographic texture between the plates (Fig. 2 e, 2 f, 3 a). Thus, more tortuous lines of crack propagation indicate the formation of bainite blocks with different crystallographic textures in these areas and demonstrate the best crack blocking action. In this case, the straight path of crack development implies the accelerated crack propagation in this area (Fig. 2 e). These facts are analyzed in detail by the EBSD method.

In the EBSD analysis of the crystallographic microtexture, grain orientations are represented as a rainbow color coding system on the studied surface and a simple way to identify the local orientation of grains (blocks, plates) in space is provided. The totality of grains forming a polycrystal as a whole consists of many elementary cells superimposed on each other. In this case, inside an elementary cell (or in a grain), one can distinguish various {001} <hkl>, {011} <hkl>, {111} <hkl>, etc. systems, along which a dislocation slip occurs. If, during cutting and further grinding of a sample along a certain section, a grain appears where the (111) plane is parallel to the section plane, then in the EBSD pattern, this grain is colored blue (Fig. 3 a). Similarly, grains with (001) are colored red, (101) – green, etc. In other words, the EBSD pattern is a distribution map of grain orientations in the plane of analysis of the section, where the {001}, {011}, {111}, etc. planes are parallel to the surface under the study (Fig. 3 a).

The EBSD analysis results clearly showed that the crack propagation nature has the straight-line sections, interruptions, and deflections (Fig. 3 a, 3 b). In particular, the transcrystalline type of crack propagation is typical for sections containing plates with {101} <0$\bar{1}$0>, {100} <001>, and {111} <$\bar{1}$00> orientations (Fig. 3 a). In this case, the intercrystalline type of crack propagation was identified for the bainite blocks belonging to the {122} <2$\bar{1}$0>, {111} <$\bar{1}$00>, {012} <$\bar{1}\bar{1}$0>, and {100} <001> orientations. CSL

grain boundaries between the adjacent plates (laths) demonstrated a significant influence on the crack development nature. The conditions for the formation of CSL grain boundaries in the steel bainitic structure are studied in most detail in the works [22–24]. In particular, it is shown that on CSL grain boundaries of the Σ 3, Σ 11, Σ 25b, Σ 33c, and Σ 41c types, the intense phase transformations begin according to the γ→α scheme during the formation of the steel bainitic structure [22]. It is noted that CSL grain boundaries of the Σ 3, Σ 11, and Σ 33c type are formed predominantly between parallel plates in a martensitic bundle and/or in a bainitic block [22; 23], while the Σ 25b type is characteristic of the martensitic structure [22]. The study showed that the Σ 41c type occurs in triple junctions of plates (laths) in a bundle containing a low-angle boundary, and two Σ 33c-type CSL grain boundaries [23]. On the other hand, in the work [24], Σ 13 and Σ 39 type CSL grain boundaries were mainly observed on the martensite-austenite and/or bainite-austenite boundaries, and the decrease in the Σ 11 proportion was explained by a decrease in the martensite component. The type of Σ 3, Σ 11, Σ 13b, Σ 25b, Σ 29a, Σ 33c, Σ 39a, and Σ 41c CSL grain boundaries revealed in this work during the formation of the bainite structure does not contradict the literature data [22–24]. According to [22; 23], it can be argued that the intense phase transformations begin on the identified CSL boundaries. At the same time, the differences in their proportion are most likely associated with the manifestation of a structural gradient through the thickness of the coupling wall. Moreover, by changing the volume fraction of certain CSL grain boundaries, it is also possible to estimate the type of structures formed [22–24]. In particular, an increased fraction of the Σ 3 type CSL grain boundaries can be explained by a multitude of bainite blocks containing parallel plates. A growth of fraction Σ 11 near the crack is associated with a growth in the martensitic component, and the strengthening of Σ 13 and Σ 39 types of CSL indicates a growth in M/A areas in this zone.

The analysis showed that Σ 3 CSL grain boundaries between the {122} <2$\bar{1}$0> and {111} <$\bar{1}$00>, {012} <$\bar{1}\bar{1}$0>, {100} <001> upper bainite plates suppress crack development, and the presence of CSL grain boundaries of the Σ 13b, Σ 29a, and Σ 39a types, on the contrary, contribute to the accelerated propagation of microcracks. In this regard, it can be concluded that cracks tend to pass through {101} <0$\bar{1}$0>, {100} <001>, and {111} <$\bar{1}$00> plates and tend to deflect when colliding with {122} <2$\bar{1}$0>, {013} <211>, {133} <$\bar{1}\bar{2}$1>, and {3$\bar{2}\bar{6}$} <201> plates.

MAIN RESULTS AND CONCLUSIONS

The conducted research showed that when producing the PS coupling according to the GOST 31446 standard, a structural gradient is observed along the thickness of the coupling wall, which consists in the formation of plates of upper and lower bainite, martensite, and martensite-austenite areas. External loads applied to the coupling create stress concentrators at the plate boundaries and on nonmetallic inclusions, which lead to the initiation and development of cracks and subsequent failure. The analysis of microtexture studies showed significant differences in the formation of crystallographic texture associated with the presence of a structural gradient during steel tempering.

It is identified that during the PS coupling operation, the {101} <0$\bar{1}$0>, {100} <001>, {122} <2$\bar{1}$0>, {013} <211>, and {3$\bar{2}\bar{6}$} <201> orientations of bainitic plates, which are undesirable to resistance at SSC, strengthen. It is shown that the Σ 3 CSL grain boundaries between {122} <2$\bar{1}$0> and {111} <$\bar{1}$00>, {012} <$\bar{1}\bar{1}$0>, {100} <001> bainite plates demonstrate a blocking effect during microcrack propagation. In this case, Σ 13b, Σ 29a, and Σ 39a CSL grain boundaries between the bainite plates, on the contrary, accelerate the propagation of microcracks. The obtained results are important for the formation in steel of a favorable structure and crystallographic texture resistant to SSC.

REFERENCES

1. Askari M., Aliofkhazraei M., Afroukhteh S. A Comprehensive Review on Internal Corrosion and Cracking of Oil and Gas Pipelines. *Journal of Natural Gas Science and Engineering*, 2019, vol. 71, article number 102971. DOI: 10.1016/j.jngse.2019.102971.

2. Wang Z.B., Pang L., Zheng Y.G. A review on under-deposit corrosion of pipelines in oil and gas fields: Testing methods, corrosion mechanisms and mitigation strategies. *Corrosion Communications*, 2022, vol. 7, pp. 70–81. DOI: 10.1016/j.corcom.2022.03.007.

3. Vyboyshchik M.A., Ioffe A.V. Scientific basis of development and the methodology of creation of steels for the production of oilfield casing and tubular goods with the increased strength and corrosion resistance. *Vektor nauki Tolyattinskogo gosudarstvennogo universiteta*, 2019, no. 1, pp. 13–20. DOI: 10.18323/2073-5073-2019-1-13-20.

4. Tkacheva V.E., Markin A.N., Kshnyakin D.V., Maltsev D.I., Nosov V.V. Corrosion of downhole equipment in hydrogen sulfur-containing environments. *Praktika protivokorrozionnoy zashchity*, 2021, vol. 26, no. 2, pp. 7–26. DOI: 10.31615/j.corros.prot.2021.100.2-1.

5. Sitdikov V.D., Nikolaev A.A., Ivanov G.V., Makatrov A.K., Malinin A.V. Microstructure and crystallographic structure of ferritic steel subjected to stress-corrosion cracking. *Letters on Materials*, 2022, vol. 12, no. 1, pp. 65–70. DOI: 10.22226/2410-3535-2022-1-65-70.

6. Tale S., Ahmed R.M., Elgaddafi R.M., Teodoriu C. Sulfide Stress Cracking of C-110 Steel in a Sour Environment. *Corrosion and Materials Degradation*, 2021, vol. 2, no. 3, pp. 376–396. DOI: 10.3390/cmd2030020.

7. Cheng Y. *Frank. Stress Corrosion Cracking of Pipelines*. Great Britain, Wiley Publ., 2013. 288 p.

8. Zhou Y. *Pipeline and Energy Plant Piping: Design and Technology*. Netherlands, Elsevier Science Publ., 2013. 392 p.

9. Sitdikov V.D., Nikolaev A.A., Makatrov A.K., Malinin A.V., Filyaeva I.M., Mironov I.V. An integrated approach to identifying causes and mechanisms of destruction of steel tubing couplings. *Neftyanoe khozyaystvo*, 2022, no. 6, pp. 48–51. EDN: HKAMHC.

10. Ren J.-Y., Li C.-S., Han Y., Li E., Gao C., Qiu C. Effect of initial martensite and tempered carbide on mechanical properties of 3Cr2MnNiMo mold steel. *Materials Science and Engineering: A*, 2021, vol. 812, article number 1410801. DOI: 10.1016/j.msea.2021.141080.

11. Ohaeri E., Eduok U., Szpunar J. Hydrogen related degradation in pipeline steel: A review. *International Journal of Hydrogen Energy*, 2018, vol. 43, no. 31, pp. 14584–14617. DOI: 10.1016/j.ijhydene.2018.06.064.

12. Pourazizi R., Mohtadi-Bonab M.A., Szpunar J.A. Investigation of different failure modes in oil and natural gas pipeline steels. *Engineering Failure Analysis*, 2020, vol. 109, article number 104400. DOI: 10.1016/j.engfailanal.2020.104400.

13. Arafin M.A., Szpunar J.A. A new understanding of intergranular stress corrosion cracking resistance of pipeline steel through grain boundary character and crystallographic texture studies. *Corrosion Science*, 2009, vol. 51, no. 1, pp. 119–128. DOI: 10.1016/j.corsci.2008.10.006.

14. Liu J., Sun J., Wei S., Lu S. The Effect of Nickel Contents on the Microstructure Evolution and Toughness of 800 MPa Grade Low Carbon Bainite Deposited Metal. *Crystals*, 2021, vol. 11, no. 6, article number 709. DOI: 10.3390/cryst11060709.

15. Zheng H., Fu L., Ji X., Ding Y., Wang W., Wen M., Shan A. Microstructural evolution and mechanical property of ultrafine-grained pearlitic steel by cold rolling: The influence of cementite morphology. *Materials Science and Engineering: A*, 2021, vol. 824, article number 141860. DOI: 10.1016/j.msea.2021.141860.

16. Müller M., Britz D., Ulrich L., Staudt T., Mücklich F. Classification of Bainitic Structures Using Textural Parameters and Machine Learning Techniques. *Metals*, 2020, vol. 10, no. 5, article number 630. DOI: 10.3390/met10050630.

17. Qian L., Li Z., Wang T., Li D., Zhang F., Meng J. Roles of pre-formed martensite in below-Ms bainite formation, microstructure, strain partitioning and impact absorption energies of low-carbon bainitic steel. *Journal of Materials Science & Technology*, 2022, vol. 96, pp. 69–84. DOI: 10.1016/j.jmst.2021.05.002.

18. Pak J.H., Bhadeshia H.K.D.H., Karlsson L., Keehan E. Coalesced bainite by isothermal transformation of reheated weld metal. *Science and Technology of Welding and Joining*, 2008, vol. 13, no. 7, pp. 593–597. DOI: 10.1179/136217108X338926.

19. Zajac S., Schwinn V., Tacke K.-H. Characterisation and Quantification of Complex Bainitic Microstructures in High and Ultra-High Strength Linepipe Steels. *Materials Science Forum*, 2005, vol. 500-501, pp. 387–394. DOI: 10.4028/www.scientific.net/MSF.500-501.387.

20. Rampelberg C., Allain S.Y.P., Geandier G., Teixiera J., Lebel F., Sourmail T. Carbide-Free Bainite Transformations Above and Below Martensite Start Temperature Investigated by In-Situ High-Energy X-Ray Diffraction. *JOM: The Journal of The Minerals, Metals & Materials Society*, 2021, vol. 73, no. 11, pp. 3181–3194. DOI: 10.1007/s11837-021-04903-8.

21. Sun Y., Wang Q., Gu S., He Z., Wang Q., Zhang F. Sulfide Stress Cracking Behavior of a Martensitic Steel Controlled by Tempering Temperature. *Materials (Basel)*, 2018, vol. 11, no. 3, article number 412. DOI: 10.3390/ma11030412.

22. Lobanov M.L., Borodina M.D., Danilov S.V., Pyshmintsev I.Y., Struin A.O. Texture inheritance on phase transition in low-carbon, low-alloy pipe steel after thermomechanical controlled processing. *Steel in Translation*, 2017, vol. 47, no. 11, pp. 710–716. DOI: 10.17073/0368-0797-2017-11-910-918.

23. Lobanov M.L., Rusakov G.M., Redikul'tsev A.A., Belikov S.V., Karabanalov M.S., Struina E.R., Gervas'ev A.M. Investigation of special misorientations in lath martensite of low-carbon steel using the method of orientation microscopy. *The Physics of Metals and Metallography*, 2016, vol. 117, no. 3, pp. 254–259. DOI: 10.7868/S0015323016030086.

24. Song T., Cooman B.C.D. Martensite Nucleation at Grain Boundaries Containing Intrinsic Grain Boundary Dislocations. *ISIJ International*, 2014, vol. 54, no. 10, pp. 2394–240. DOI: 10.2355/isijinternational.54.2394

СПИСОК ЛИТЕРАТУРЫ

1. Askari M., Aliofkhazraei M., Afroukhteh S. A Comprehensive Review on Internal Corrosion and Cracking of Oil and Gas Pipelines // Journal of Natural Gas Science and Engineering. 2019. Vol. 71. Article number 102971. DOI: 10.1016/j.jngse.2019.102971.

2. Wang Z.B., Pang L., Zheng Y.G. A review on under-deposit corrosion of pipelines in oil and gas fields: Testing methods, corrosion mechanisms and mitigation strategies // Corrosion Communications. 2022. Vol. 7. P. 70–81. DOI: 10.1016/j.corcom.2022.03.007.

3. Выбойщик М.А., Иоффе А.В. Научные основы разработки и методология создания сталей для производства нефтепромысловых труб повышенной прочности и коррозионной стойкости // Вектор науки Тольяттинского государственного университета. 2019. № 1. С. 13–20. DOI: 10.18323/2073-5073-2019-1-13-20.

4. Ткачева В.Э., Маркин А.Н., Кшнякин Д.В., Мальцев Д.И., Носов В.В. Коррозия внутрискважинного оборудования в сероводородсодержащих средах // Практика противокоррозионной защиты. 2021. Т. 26. № 2. С. 7–26. DOI: 10.31615/j.corros.prot.2021.100.2-1.

5. Sitdikov V.D., Nikolaev A.A., Ivanov G.V., Makatrov A.K., Malinin A.V. Microstructure and crystallographic structure of ferritic steel subjected to stress-corrosion cracking // Letters on Materials. 2022. Vol. 12. № 1. P. 65–70. DOI: 10.22226/2410-3535-2022-1-65-70.

6. Tale S., Ahmed R.M., Elgaddafi R.M., Teodoriu C. Sulfide Stress Cracking of C-110 Steel in a Sour Environment // Corrosion and Materials Degradation. 2021. Vol. 2. № 3. P. 376–396. DOI: 10.3390/cmd2030020.

7. Cheng Y. Frank. Stress Corrosion Cracking of Pipelines. Great Britain: Wiley, 2013. 288 p.

8. Zhou Y. Pipeline and Energy Plant Piping: Design and Technology. Netherlands: Elsevier Science, 2013. 392 p.

9. Ситдиков В.Д., Николаев А.А., Макатров А.К., Малинин А.В., Филяева И.М., Миронов И.В. Комплексный подход к выявлению причин и механизмов разрушения стальных насосно-компрессорных муфт // Нефтяное хозяйство. 2022. № 6. С. 48–51. EDN: НКАМНС.

10. Ren J.-Y., Li C.-S., Han Y., Li E., Gao C., Qiu C. Effect of initial martensite and tempered carbide on mechanical properties of 3Cr2MnNiMo mold steel // Materials Science and Engineering: A. 2021. Vol. 812. Article number 1410801. DOI: 10.1016/j.msea.2021.141080.

11. Ohaeri E., Eduok U., Szpunar J. Hydrogen related degradation in pipeline steel: A review // International Journal of Hydrogen Energy. 2018. Vol. 43. № 31. P. 14584–14617. DOI: 10.1016/j.ijhydene.2018.06.064.

12. Pourazizi R., Mohtadi-Bonab M.A., Szpunar J.A. Investigation of different failure modes in oil and natural gas pipeline steels // Engineering Failure Analysis. 2020. Vol. 109. Article number 104400. DOI: 10.1016/j.engfailanal.2020.104400.

13. Arafin M.A., Szpunar J.A. A new understanding of intergranular stress corrosion cracking resistance of pipeline steel through grain boundary character and crystallographic texture studies // Corrosion Science. 2009. Vol. 51. № 1. P. 119–128. DOI: 10.1016/j.corsci.2008.10.006.

14. Liu J., Sun J., Wei S., Lu S. The Effect of Nickel Contents on the Microstructure Evolution and Toughness of 800 MPa Grade Low Carbon Bainite Deposited Metal // Crystals. 2021. Vol. 11. № 6. Article number 709. DOI: 10.3390/cryst11060709.

15. Zheng H., Fu L., Ji X., Ding Y., Wang W., Wen M., Shan A. Microstructural evolution and mechanical property of ultrafine-grained pearlitic steel by cold rolling: The influence of cementite morphology // Materials Science and Engineering: A. 2021. Vol. 824. Article number 141860. DOI: 10.1016/j.msea.2021.141860.

16. Müller M., Britz D., Ulrich L., Staudt T., Mücklich F. Classification of Bainitic Structures Using Textural Parameters and Machine Learning Techniques // Metals. 2020. Vol. 10. № 5. Article number 630. DOI: 10.3390/met10050630.

17. Qian L., Li Z., Wang T., Li D., Zhang F., Meng J. Roles of pre-formed martensite in below-Ms bainite formation, microstructure, strain partitioning and impact absorption energies of low-carbon bainitic steel // Journal of Materials Science & Technology. 2022. Vol. 96. P. 69–84. DOI: 10.1016/j.jmst.2021.05.002.

18. Pak J.H., Bhadeshia H.K.D.H., Karlsson L., Keehan E. Coalesced bainite by isothermal transformation of reheated weld metal // Science and Technology of Welding and Joining. 2008. Vol. 13. № 7. P. 593–597. DOI: 10.1179/136217108X338926.

19. Zajac S., Schwinn V., Tacke K.-H. Characterisation and Quantification of Complex Bainitic Microstructures in High and Ultra-High Strength Linepipe Steels // Materials Science Forum. 2005. Vol. 500-501. P. 387–394. DOI: 10.4028/www.scientific.net/MSF.500-501.387.

20. Rampelberg C., Allain S.Y.P., Geandier G., Teixiera J., Lebel F., Sourmail T. Carbide-Free Bainite Transformations Above and Below Martensite Start Temperature Investigated by In-Situ High-Energy X-Ray Diffraction // JOM: The Journal of The Minerals, Metals & Materials Society. 2021. Vol. 73. № 11. P. 3181–3194. DOI: 10.1007/s11837-021-04903-8.

21. Sun Y., Wang Q., Gu S., He Z., Wang Q., Zhang F. Sulfide Stress Cracking Behavior of a Martensitic Steel Controlled by Tempering Temperature // Materials (Basel). 2018. Vol. 11. № 3. Article number 412. DOI: 10.3390/ma11030412.

22. Лобанов М.Л., Бородина М.Д., Данилов С.В., Пышминцев И.Ю., Струин А.О. Текстурная наследственность при фазовых превращениях в малоуглеродистой низколегированной трубной стали после контролируемой термомеханической обработки // Известия высших учебных заведений. Черная метал-

лургия. 2017. Т. 60. № 11. С. 910–918. DOI: 10.17073/0368-0797-2017-11-910-918.

23. Лобанов М.Л., Русаков Г.М., Редикульцев А.А., Беликов С.В., Карабаналов М.С., Струина Е.Р., Гервасьев А.М. Исследование специальных разориентаций в реечном мартенсите низкоуглеродистой стали методом ориентационной микроскопии // Физика металлов и металловедение. 2016. Т. 117. № 3. С. 266–271. DOI: 10.7868/S0015323016030086.

24. Song T., Cooman B.C.D. Martensite Nucleation at Grain Boundaries Containing Intrinsic Grain Boundary Dislocations // ISIJ International. 2014. Vol. 54. № 10. P. 2394–240. DOI: 10.2355/isijinternational.54.2394.

Особенности микроструктуры и микротекстуры среднеуглеродистой стали, подвергнутой сероводородному растрескиванию под напряжением

© 2023

*Малинин Андрей Владимирович**[1,3], кандидат технических наук, заместитель генерального директора
Ситдиков Виль Даянович[1,4], доктор физико-математических наук, заведующий лабораторией
Ткачева Валерия Эдуардовна[1,5], кандидат технических наук, доцент, главный специалист
Макатров Артем Константинович[1,6], кандидат технических наук, начальник управления
Валекжанин Илья Владимирович[1,7], начальник отдела
Маркин Андрей Николаевич[2], кандидат технических наук, доцент кафедры «Нефтегазовое дело»

[1]*ООО «РН-БашНИПИнефть», Уфа (Россия)*
[2]*Филиал Тюменского индустриального университета в г. Нижневартовске, Нижневартовск (Россия)*

*E-mail: MalininAV@bnipi.rosneft.ru

[3]ORCID: https://orcid.org/0000-0003-1185-5648
[4]ORCID: https://orcid.org/0000-0002-9948-1099
[5]ORCID: https://orcid.org/0000-0001-6927-9781
[6]ORCID: https://orcid.org/0000-0002-2822-9072
[7]ORCID: https://orcid.org/0000-0001-9472-2968

Аннотация: Повышение стойкости стальных изделий к сероводородному растрескиванию под напряжением (СРН) является одной из актуальных тем нефтегазовой промышленности. Среди различных факторов, определяющих устойчивость материала к СРН, выделяется структурно-фазовое состояние самого материала и связанная с ним кристаллографическая текстура. В данной работе эти особенности материала проанализированы методами растровой электронной микроскопии (РЭМ), просвечивающей электронной микроскопии (ПЭМ) и микрорентгеновской дифракции обратно рассеянных электронов (ДОРЭ). В качестве материала исследований выбрана муфта эксплуатационной колонны (ЭК), которая разрушилась по механизму водородного охрупчивания и последующего СРН. Муфта ЭК изготовлена из среднеуглеродистой стали. Впервые методом РЭМ по расположению и взаимной ориентации частиц цементита (Fe_3C) при больших увеличениях продемонстрированы возможности идентификации в сталях составляющих верхнего бейнита, нижнего бейнита и отпущенного мартенсита. Наличие обнаруженных структурных составляющих стали подтверждено методом ПЭМ. Методом ДОРЭ проведены детальные исследования микротекстуры для установления типа и характера распространения микротрещины. Установлено, что процессы водородного охрупчивания и последующее СРН приводят к формированию {101} <0$\overline{1}$0>, {100} <001>, {122} <2$\overline{1}$0>, {013} <211>, {111} <$\overline{1}$00>, {133} <$\overline{1}$$\overline{2}$1>, {3$\overline{2}$$\overline{6}$} <201> ориентаций зерен. Показано, что усиление ориентировок {001} <110>, {100} <001>, {112} <111> и {133} <$\overline{1}$$\overline{2}$1> типов ухудшают стойкость материала к СРН. Методом ДОРЭ-анализа оценено влияние специальных границ зерен на характер распространения микротрещины. Обнаружено, что специальные границы Σ 3 между {122} <2$\overline{1}$0> и {111} <$\overline{1}$00>, {012} <$\overline{1}$$\overline{1}$0>, {100} <001> пластинами верхнего бейнита тормозят развитие микротрещины, а границы Σ 13b, Σ 29a и Σ 39a, наоборот, способствуют ускоренному распространению микротрещин. Для сравнительного анализа проведены аналогичные исследования в неразрушенной (исходной) муфте до эксплуатации.

Ключевые слова: среднеуглеродистая сталь; бейнитная микроструктура; сероводородное растрескивание под напряжением; кристаллографическая текстура.

Для цитирования: Малинин А.В., Ситдиков В.Д., Ткачева В.Э., Макатров А.К., Валекжанин И.В., Маркин А.Н. Особенности микроструктуры и микротекстуры среднеуглеродистой стали, подвергнутой сероводородному растрескиванию под напряжением // Frontier Materials & Technologies. 2023. № 1. С. 33–44. DOI: 10.18323/2782-4039-2023-1-33-44.